# Predicting Dendritic Growth in Solidification Processes Using Surrogate Models

Ali Tayyar, Georges Sakr, Zeinab Khanafer

MECH 798M, Mechanical Engineering Department, American University of Beirut

Advisor: Dr. Joseph Bakarji

## Abstract

Dendritic solidification is a fundamental phenomenon in materials science, shaping the microstructure of metals, alloys, and energy storage systems. While phase-field models offer high-fidelity simulations of this process, their substantial computational cost hinders scalability and real-time applications. In this project, we develop a deep learning-based surrogate model capable of accurately predicting dendritic growth patterns from physical input parameters. Training data is generated using a FiPy-based numerical solver that captures the coupled evolution of the phase field ($\xi$) and undercooling ($\Delta T$). Our surrogate achieves substantial speed-up while preserving physical consistency. We further explore optimization strategies to identify input configurations that yield targeted fractal morphologies, paving the way for microstructure-aware design in manufacturing and energy applications.

## 1 Introduction and Motivation

Dendritic growth is a pivotal phenomenon in materials science, shaping the microstructural characteristics of metals, alloys, and energy storage systems. The intricate patterns of dendrites profoundly affect mechanical strength, thermal properties, and electrochemical efficiency. Effective control of dendritic structures is critical for enhancing metallurgical solidification processes and preventing detrimental effects, such as dendrite-related failures in rechargeable batteries [1, 2]. Among computational techniques for studying dendritic evolution, *phase-field modeling* (PFM) stands out for its ability to simulate complex interface dynamics without explicitly tracking boundaries [3]. However, the computational intensity of PFM, driven by the need for high-resolution spatial and temporal grids to model interfaces and temperature fields [2], poses significant challenges. To address this, machine learning (ML) approaches provide a compelling solution by developing surrogate models trained on high-fidelity PFM data to predict dendritic growth patterns efficiently [4, 5]. This project focuses on constructing an ML-based surrogate model to forecast dendritic morphologies during solidification, using training data from a FiPy-based PFM framework, specifically the anisotropy example [6]. The model simulates the dynamics of the phase field ($\xi$) and undercooling ($\Delta T$), as illustrated in Figure 1. Furthermore, we study two physical characteristics of dendritic growth to determine the ideal dendrite configurations for various applications, ensuring both computational efficiency and adherence to physical principles.
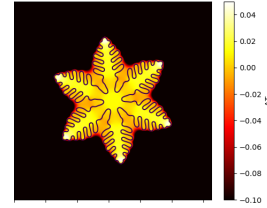


Figure 1: Dendritic growth simulation with phase-field $\xi$ and temperature $\Delta T$ [6]

## 2 Related Work

Phase-field modeling (PFM) is a cornerstone in the simulation of solidification processes, particularly for capturing complex phenomena such as anisotropic dendritic growth [7, 8]. Classic models developed by [7] and [8] have demonstrated the efficacy of PFM in simulating dendritic growth, with Kobayashi's work focusing on numerical simulations including anisotropy, and Warren *et al.* extending these models to polycrystalline materials. However, the high computational cost associated with these simulations has spurred the development of surrogate models [9, 5, 10]. [10] introduced stochastic multi-fidelity Gaussian process models to enhance the efficiency of such simulations, while [5] proposed deep operator networks as a novel approach for phase-field surrogate modeling, specifically for metal grain growth during solidification. More recently, [9] applied physics-informed neural networks (PINNs) to solve coupled Allen-Cahn and Cahn-Hilliard phase field equations, ensuring that the neural surrogates maintain physical consistency. These advancements underscore the ongoing efforts to make phase-field modeling more computationally tractable while preserving its accuracy and physical relevance.

## 3 Problem Formulation

We aim to approximate the final/ full dendritic morphology using a surrogate model conditioned on simulation parameters. Let $\vec{x} = [\Delta T_0, c, N, \theta, r_0, t]$ denote the input parameter vector, where:

- $\Delta T_0$: is the initial undercooling

- $c$: is the anisotropy strength

- $N$: is the number of seed points,

- $\theta$: is the orientation of anisotropy

- $r_0$: is the initial seed radius

The output of the simulation is the spatio-temporal evolution of the phase field $\xi(t, x, y)$, which satisfies the following PDE system:

$$\frac{\partial \Delta T}{\partial t} = D_T \nabla^2 \Delta T + \frac{\partial \xi}{\partial t}, \tag{1}$$

$$\tau \frac{\partial \xi}{\partial t} = \nabla \cdot (D \nabla \xi) + (\xi - 0.5) \tag{2}$$
$$- \frac{\kappa_1}{\pi} \arctan(\kappa_2 \Delta T)(1 - \xi),$$

where $\tau$ is the relaxation time, and $D$ is the anisotropic diffusivity tensor given by:

$$D = \alpha^2 (1 + c\beta) \begin{bmatrix} 1 + c\beta & -c\frac{\partial \beta}{\partial \psi} \\ c\frac{\partial \beta}{\partial \psi} & 1 + c\beta \end{bmatrix}. \tag{3}$$

Our goal is to learn a surrogate model $\mathcal{F}_\theta(x)$ such that:

$$\hat{\xi}(x, y, t) \approx \mathcal{F}_\theta(\vec{x}),$$

where $\hat{\xi}$ is the phase field morphology, and $\theta$ denotes the trainable parameters of the model.

# 4 Methodology

## 4.1 Data Generation

We used a simulator that relies on the FiPy-Finite Volume method to simulate a 2D phase-field model with varied parameters [6]: $\Delta T_0$, $c$, $N$, $\theta$, and $r_0$. Each simulation generated a spatio-temporal field $\xi(t, x, y)$, for different $\vec{x} \in \mathbb{R}^5$ where $\vec{x}$ denote the vector of physical input parameters:

$$\vec{x} = [\Delta T_0,\ c,\ N,\ \theta,\ r_0]^\top.$$

The system is solved on a uniform grid of $250 \times 250$ cells. Each simulation runs for 750 time steps, outputting snapshots of the phase field $\xi(t, x, y)$ every 25 time steps. The evolution is governed by the coupled equations for $\xi$ and $\Delta T$, under periodic or Dirichlet boundary conditions.

## 4.2 Last Frame Analysis $(\hat{\xi}_T(t_{final}, x, y):$ Models Used:

We trained several models, including :

- **Linear Regression**: $\hat{\xi}_T = XB + \varepsilon$

- **Polynomial Regression**: $\hat{\xi}_T = \Phi(X)B + \varepsilon$

- **CNN**: 9-layers network trained to map $x$ to $\hat{\xi}$ image (only for the last frame)

- **PINN**: 3-layers network with an added physics-based residual in the loss.

We did **Data Splitting, such that:** 80% training, 20%. Also, we defined a **Loss Metrics**, which uses a Pixel-wise MSE for morphology and took its average, in addition to physics residual for PINNs.

## 4.3 All-Frame Surrogate Modeling:

While initial surrogate models focused solely on predicting the final frame of the phase field $\hat{\xi}_T(x, y) = \hat{\xi}(t_{\text{final}}, x, y)$, we extend this formulation to model the full spatio-temporal evolution of the system.

We use a *Convolutional Neural Network* (CNN), such that an input $\vec{x}$ We define the output tensor $\hat{\xi} \in \mathbb{R}^{N_x \times N_y \times N_t}$, where $N_x = N_y = 250$ is the spatial resolution and $N_t = 30$ corresponds to 30 stored frames (sampled from 750 time steps).

The model is composed of $L$ layers, each applying a 2D convolution followed by a non-linear activation. The hidden representations are defined recursively as:

$$h^{(l+1)} = \sigma\left(W^{(l)} * h^{(l)} + b^{(l)}\right), \text{ for } l = 0, \ldots, L-1, \tag{4}$$

where $*$ denotes the convolution operator, $W^{(l)}$ and $b^{(l)}$ are the trainable kernel weights and biases at layer $l$, and $\sigma(\cdot)$ is the ReLU activation function. The input to

$$\vec{x} \xrightarrow{\textbf{CNN}} \hat{\xi}(t, \mathbf{x}, \mathbf{y})$$
$$\mathbb{R}^{5 \times 1} \qquad\qquad \mathbb{R}^{250 \times 250 \times 30}$$

the network is the vector $\vec{x}$, passed through a fully connected embedding layer and reshaped into a spatial grid. This latent grid is then upsampled through a sequence of convolutional and interpolation blocks to produce the final output tensor $\hat{\xi}$.

## 4.4 Loss Functions

For training, we use the Mean Squared Error computed over all pixels, averaging over the entire batch. Given predicted and ground truth sequences of phase field morphologies $\hat{\xi}^{(i)} = \{\hat{\xi}_t^{(i)}\}_{t=1}^T$ and $\xi^{(i)} = \{\xi_t^{(i)}\}_{t=1}^T$ for the $i$-th training example, the loss is defined as:

$$\mathcal{L}_{\text{MSE}} = \frac{1}{n_x n_y} \sum_{i=1}^N \sum_{t=1}^T \left\| \hat{\xi}_t^{(i)} - \xi_t^{(i)} \right\|_2^2, \tag{5}$$

Where $n_x \times n_y$ is the spatial resolution of each frame. We also added the MSE of all the frames and averaged over them when dealing with all of them.

Additionally, we explore physics-informed terms in later stages of the report, which penalize the surrogate model for violating the governing PDE residuals during training.

The physics-informed loss ($\mathcal{L}_{\text{PDE}}$) is defined as the mean squared residual of the phase-field equation, enforcing

the predicted fields $\hat{\xi}$ and $\hat{T}$ to satisfy the governing partial differential equation. It is given by:

$$\mathcal{L}_{\text{PDE}} = \frac{1}{N} \sum_{i,t,x,y} (\tau \frac{\partial \hat{\xi}}{\partial t} - \nabla^2 \hat{\xi} ...$$

$$... - \left( \hat{\xi} - 0.5 - \frac{k_1}{\pi} \arctan(k_2 \hat{T}) \right) (1 - \hat{\xi}))^2 \quad (6)$$

where $\hat{\xi}$ and $\hat{T}$ are the predicted phase and temperature fields, $\tau$, $k_1$, and $k_2$ are model parameters, $\frac{\partial \hat{\xi}}{\partial t}$ is the temporal derivative (via forward finite difference), $\nabla^2 \hat{\xi}$ is the spatial Laplacian (via a 5-point stencil), and $N$ is the total number of residual points over batch $i$, time $t$, and spatial dimensions $x, y$.

## 5 Results and Analysis

### 5.1 Final Frame Analysis

#### 5.1.1 Evaluation of Regression Predictions:

We begin by evaluating and analyzing the models used to predict the final frame of the surrogate output, as discussed in Section 4.2. Both linear and polynomial regression models achieved low MSE in both the training and testing datasets 5.1.2. However, reconstructing final phase-field frames revealed a notable difference in performance. The polynomial regression model successfully reproduced the global morphology and localized solidification behavior, accurately. In contrast, the linear regression model yielded outputs that visually resembled an average over multiple realizations 2.
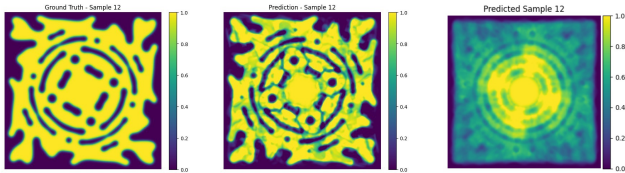


(a) Ground Truth  (b) Polynomial Regression  (c) Linear Regression

Figure 2: Comparison for sample $\hat{\xi}_{012}$ predictions. The polynomial model captures dendritic features with high fidelity, while the linear model shows mode averaging and loss of spatial detail.

To further investigate the differences between the linear and polynomial regression models, we performed a singular value decomposition on the learned coefficient matrix $B$ as defined in 4.2, in the regression models. The decomposition expresses the coefficient matrix as $B = U\Sigma V^\top$, where $U$ encodes spatial modes (analogous to eigenframes), $\Sigma$ contains the singular values, and $V^\top$ captures linear combinations of input parameters that activate these spatial responses.

Remarkably, the first two singular values in the linear regression model accounted for over 85% of the total energy. This indicates that the output fields are predominantly driven by just two dominant spatial modes, which

explains the averaging observed in the reconstructions. In contrast, the polynomial regression model exhibited a more distributed singular value spectrum, suggesting a richer basis set that better captures the diversity of dendritic morphologies.

Additionally, in the linear regression model, the first two principal input directions—corresponding to the highest singular values—were predominantly linear combinations of $\Delta T_0$ (undercooling) and $c$ (anisotropy strength). These parameters are primarily responsible for controlling the extent and rate of dendritic growth rather than the intricate morphological features or branching geometry. In contrast, the polynomial regression model exhibited more complex input mode combinations involving multiple parameters, allowing it to better encode interactions responsible for orientation, branching symmetry, and seed-induced features.

#### 5.1.2 Quantitative Comparison of Surrogate Models

We summarize the predictive performance of the surrogate models using the Mean Squared Error (MSE) on both training and testing datasets. All models were trained to predict the final phase-field frame, and hyperparameters (e.g., polynomial degree) were selected to minimize test error.

Table 1: Mean Squared Error (MSE) comparison of surrogate models.

| Model | Train MSE | Test MSE |
| --- | --- | --- |
| Poly. Reg. (Deg. 7) | 0.00134 | 0.03288 |
| Linear Regression | 0.05929 | 0.05676 |
| CNN | 0.01928 | 0.03431 |
| PINN | 0.00345 | 0.01947 |

The results indicate that PINNs achieved the best generalization performance, followed closely by CNNs and high-degree polynomial regression.

### 5.2 All Frame Analysis:

#### 5.2.1 Evaluation of CNN Predictions

To evaluate the learned surrogate's ability to approximate the full evolution of dendritic growth, we visualize predicted versus ground truth morphologies at selected time frames: $t = 0$, $10$, and $29$, as shown in Figure (3).

The model was trained for 200 epochs using the Adam optimizer with a batch size of 16 and learning rate $\alpha = 1e^{-3}$. The validation mean squared error (MSE) progressively decreased as shown in figure (4) and reached a minimum value of:

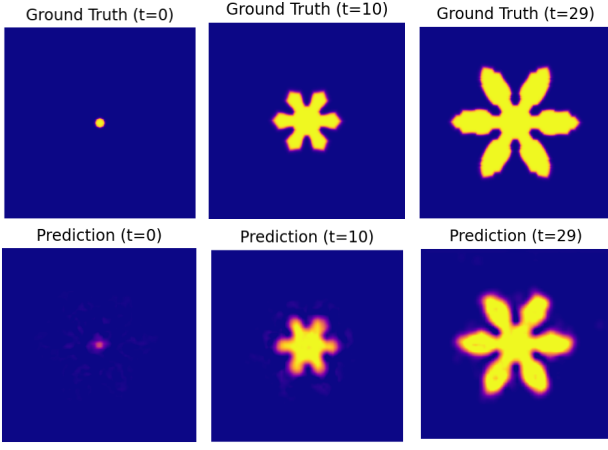$$\text{MSE}_{\text{val}} = 7.79 \times 10^{-3} \quad (7)$$

Figure 3: CNN predictions vs. ground truth evolution for a branched dendritic morphology at selected time frames $t = 0, 10, 29$.
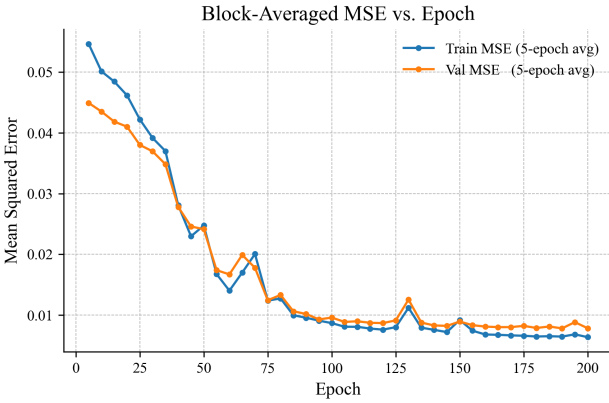


Figure 4: Block-averaged training and validation MSE vs. epoch (5-epoch window smoothing).

#### 5.2.2 Evaluation of Physics Informed Neural Networks PINNs

In addition to training our model using CNNs, we have augmented the mean-squared error with a physics-informed term which is defined as the squared residual of the governing PDE. We aswell used Adam optimizer and trained it for 50 epochs with a batch size of 8 and a learning rate of $\alpha = 1 \times 10^{-3}$, reducing the average squared PDE residual to a physics loss of:

$$\text{Physics}_{\text{val}} = 4.7 \times 10^{-4} \tag{8}$$

Figure (5) compares a standard CNN and a physics-informed CNN, highlighting their architectural differences in predicting dendritic growth patterns.

## 6 Morphology Quantification and Dimensionless Analysis

To systematically interpret and compare dendritic morphologies, we define two key scalar metrics: the *solid fraction* and a dimensionless measure of *interface complexity* (branchiness).
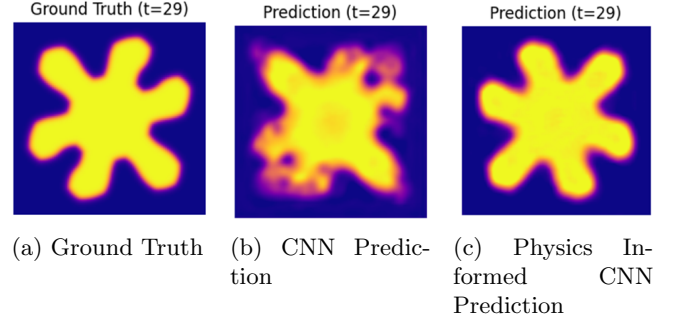


(a) Ground Truth  (b) CNN Prediction  (c) Physics Informed CNN Prediction

Figure 5: Comparison of the learned $\hat{\xi}_T(t, x, y)$.

### 6.1 Solid Fraction (SF)

The solid fraction $SF$ is defined as the normalized integral of the phase field over the spatial domain $\Omega$ at the final simulation time $t_{\text{final}}$:

$$SF = \frac{1}{|\Omega|} \int_{\Omega} \hat{\xi}(t_{\text{final}}, x, y) \, d\Omega, \tag{9}$$

where $|\Omega|$ denotes the area of the spatial domain, and $\hat{\xi}(t_{\text{final}}, x, y) \in [0, 1]$ is the phase field at final time, with values close to 1 representing solid regions.

In our discrete implementation, this becomes:

$$SF \approx \frac{1}{N_x N_y} \sum_{i=1}^{N_x} \sum_{j=1}^{N_y} \hat{\xi}(t_{\text{final}}, x_i, y_j), \tag{10}$$

where $(N_x, N_y)$ are the number of spatial grid points in the $x$ and $y$ directions.

We performed a random search over the input parameter space $\vec{x} = [\Delta T_0, c, N, \theta, r_0]$ to identify regions that yield high solid fractions. While more sophisticated optimization methods such as Bayesian optimization or genetic algorithms are suitable for such tasks, our focus here was proof-of-concept exploration.

The maximum observed solid fraction was:

$$SF^* = 0.7354 \text{ for input } \vec{x}^* = \big[\Delta T_0 = -0.843,$$
$$c = 0.037, \, N = 10, \, \theta = 69.08°, \, r_0 = 0.195\big]. \tag{11}$$

This parameter configuration corresponds to a case with high undercooling and moderate anisotropy, which together promote rapid interface advancement and dense solidification. The highest SF is shown in figure (6)

### 6.2 Branchiness

We define *branchiness*, denoted $BR$, as a scalar measure of the interfacial complexity of the dendritic structure. It is computed as the total variation norm of the phase field $\hat{\xi}(t_{final}, x, y)$ at the final simulation time $t_{\text{final}}$, and is formally defined as:

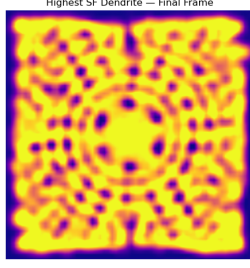$$BR = \int_{\Omega} \left\| \nabla \hat{\xi}(t_{\text{final}}, x, y) \right\|_2 \, dx \, dy, \tag{12}$$

4

Figure 6: Solid fraction ($SF^*$) variation across different input configurations. The metric quantifies the proportion of solidified material at the final simulation time.

where $\left\|\nabla\hat{\xi}\right\|_2 = \sqrt{\left(\frac{\partial\hat{\xi}}{\partial x}\right)^2 + \left(\frac{\partial\hat{\xi}}{\partial y}\right)^2}$ is the Euclidean norm of the gradient. This expression captures the cumulative interfacial activity across the domain.

In discrete form, over a uniform grid of resolution $(N_x, N_y)$, this becomes:

$$BR \approx \sum_{i=1}^{N_x}\sum_{j=1}^{N_y} \sqrt{\left(\delta_x\hat{\xi}_{i,j}\right)^2 + \left(\delta_y\hat{\xi}_{i,j}\right)^2}, \qquad (13)$$

where $\delta_x$ and $\delta_y$ denote finite-difference approximations of the spatial derivatives along $x$ and $y$, respectively. Numerically, we use central differences for interior points and one-sided differences at boundaries.

This metric favors morphologies with sharper gradients and more intricate boundaries, making it particularly sensitive to interface roughness and secondary dendrite arms.

A parameter sweep over the simulation input space yields the following extrema:

Minimum Branchiness: $\quad SF = 0.028, \quad BR = 161.3,$
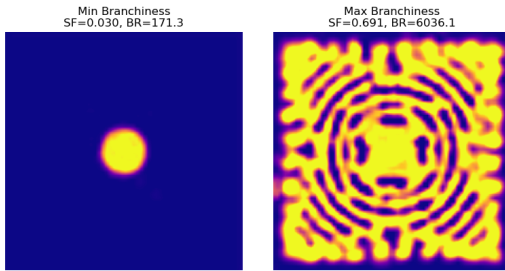Maximum Branchiness: $\quad SF = 0.686, \quad BR = 6254.7.$



Figure 7: Comparison of morphologies with minimum and maximum branchiness.

## 6.3 Dimensionless Analysis Insights: Dendricity

We observe from empirical analysis (Figure 8) that branchiness $BR$ increases with solid fraction $SF$, suggesting a power-law relationship of the form:

$$BR \sim SF^\gamma, \qquad (14)$$

where $\gamma > 1$ reflects the increased interface complexity associated with more extensive solidification. To decouple interface roughness from bulk solidification effects, we define a dimensionless metric termed **Dendricity**, denoted $D$, as:

$$D = BR^\alpha SF^\beta, \qquad (15)$$

where $\alpha$ and $\beta$ are scaling exponents empirically chosen or fit to data such that $D$ remains approximately invariant under scaling of solid fraction alone. This formulation is inspired by the Buckingham $\pi$-theorem, capturing morphology complexity independent of volume fraction.

In practice, we fix $(\alpha, \beta)$ to normalize variations across samples and analyze dendricity as a morphology classifier: Low $D$ values correspond to compact, blob-like structures. High $D$ values indicate extensive branching relative to solidified volume.

This dimensionless analysis enables better comparison across different growth regimes and guides inverse design strategies targeting morphologies with desired levels of interfacial complexity.
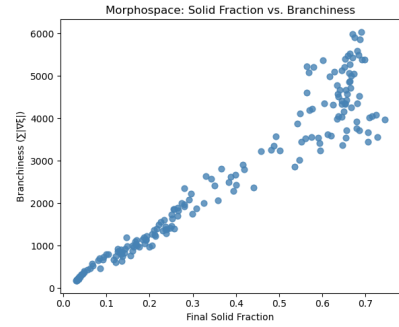


Figure 8: Morphospace plot showing the empirical relationship between solid fraction ($SF$) and branchiness ($BR$). The observed power-law trend motivates the definition of the dimensionless dendricity metric $D = BR^\alpha SF^\beta$.

Further work could extend the dendricity formulation by incorporating additional physical characteristics such as *tortuosity* ($\tau$), which reflects ion transport path complexity, and *porosity* ($\varepsilon$), representing the void fraction within the morphology. These parameters can provide deeper insight into the electrochemical performance associated with different dendritic structures. A generalized dendricity measure could then take the form:

$$D' = BR^\alpha SF^\beta \tau^\sigma ...$$

where the exponents $\alpha$, $\beta$, and $\delta$, are scaling weights that can be tuned based on empirical or computational analysis.

## 7    Conclusion and Future Work

We developed surrogate models to efficiently predict dendritic growth during solidification based on physical inputs. Starting from linear and polynomial regression, we advanced to CNNs and physics-informed neural networks (PINNs). PINNs offered the best performance, balancing accuracy with adherence to physical laws. Models were trained on FiPy-generated simulations and captured both final and full-frame morphologies.

To quantify and compare growth patterns, we used solid fraction and branchiness metrics and introduced a dimensionless dendricity measure to capture morphological complexity. These tools helped identify input regimes that yield desired structures.

Limitations include difficulty capturing fine details at later times, reliance on 2D simulations, and the added cost of physics-informed training.

Future work includes extending to 3D simulations, using active learning to reduce data demands, and balancing physics and data losses for better training. Adding tortuosity ($\tau$) and different characterization parameters to dendricity can offer a more complete picture of morphology, and could enhance surrogate models for practical use in materials and energy applications.

## GitHub Repository

MAKE SURE TO CHECK THE CODES HERE!

## References

[1] C.-H. Chen and C.-W. Pao, "Phase-field study of dendritic morphology in lithium metal batteries," *Journal of Power Sources*, vol. 484, p. 229203, 2021.

[2] M. A. Jaafar, D. R. Rousse, S. Gibout, and J.-P. Bédécarrats, "A review of dendritic growth during solidification: Mathematical modeling and numerical simulations," *Renewable and Sustainable Energy Reviews*, vol. 74, pp. 1064–1079, 2017.

[3] T. Takaki, "Phase-field modeling and simulations of dendrite growth," *ISIJ international*, vol. 54, no. 2, pp. 437–444, 2014.

[4] J. Winter, J. Kaiser, S. Adami, I. Akhatov, and N. Adams, "Stochastic multi-fidelity surrogate modeling of dendritic crystal growth," *Computer Methods in Applied Mechanics and Engineering*, vol. 393, p. 114799, 2022.

[5] D. Ciesielski, Y. Li, S. Hu, E. King, J. Corbey, and P. Stinis, "Deep operator network surrogate for phase-field modeling of metal grain growth during solidification," *Computational Materials Science*, vol. 246, p. 113417, 2025.

[6] "examples.phase.anisotropy — fipy 3.4.4 documentation." `https://www.ctcms.nist.gov/fipy/examples/phase/generated/examples.phase.anisotropy.html`. Accessed: 2025-03-21.

[7] R. Kobayashi, "Modeling and numerical simulations of dendritic crystal growth," *Physica D: Nonlinear Phenomena*, vol. 63, no. 3-4, pp. 410–423, 1993.

[8] J. A. Warren, R. Kobayashi, A. E. Lobkovsky, and W. C. Carter, "Extending phase field models of solidification to polycrystalline materials," *Acta materialia*, vol. 51, no. 20, pp. 6035–6058, 2003.

[9] N. Chen, S. Lucarini, R. Ma, A. Chen, and C. Cui, "Pf-pinns: Physics-informed neural networks for solving coupled allen-cahn and cahn-hilliard phase field equations," *Journal of Computational Physics*, p. 113843, 2025.

[10] L. Parussini, D. Venturi, P. Perdikaris, and G. E. Karniadakis, "Multi-fidelity gaussian process regression for prediction of random fields," *Journal of Computational Physics*, vol. 336, pp. 36–50, 2017.